Journal of
Materials Chemistry A

ROYAL SOCIETY
OF CHEMISTRY

PAPER

View Article Online
View Journal | View Issue

Cite this: *J. Mater. Chem. A*, 2022, **10**, 11574

Li-ion conductivity in $Li_2OHCl_{1-x}Br_x$ solid electrolytes: grains, grain boundaries and interfaces†

Hyeon Jeong Lee,[a] Brigita Darminto,[a] Sudarshan Narayanan,[a] Maria Diaz-Lopez,[b] Albert W. Xiao,[a] Yvonne Chart,[a] Ji Hoon Lee,[c] James A. Dawson[de] and Mauro Pasta*[a]

Received 22nd February 2022
Accepted 26th April 2022

DOI: 10.1039/d2ta01462a

rsc.li/materials-a

In this study, we conduct a comprehensive investigation of the effect of grain, grain boundary and interfacial resistance on the total Li-ion conductivity in $Li_2OHCl_{1-x}Br_x$ antiperovskite solid electrolytes. We highlight how the thermal expansion coefficient can serve as an indicator for the presence of structural defects, which are difficult to probe directly with X-ray techniques, and their effect on bulk Li-ion conduction. The detrimental effect of grain boundaries on ionic conductivity is investigated by atomistic calculations and validated experimentally by electrochemical impedance spectroscopy on pellets with controlled grain size. The effect of composition on interfacial resistance is probed by electrochemical impedance spectroscopy and X-ray photoelectron spectroscopy. These insights provide design principles to improve Li-ion conductivity in lithium hydroxide halide antiperovskites.

Introduction

Solid-state batteries have received widespread attention due to the increasing demand for improvements on commercial Li-ion batteries in terms of energy density, operating temperature range, and safety.[1,2] Unfortunately, the practical implementation of solid-state batteries has been hindered by their limited Li-ion conductivity, which is still lower than that of conventional batteries based on liquid electrolytes.[3,4] The total resistivity of solid-state batteries (R_{total}) with crystalline solid electrolytes is determined by the resistivities of the grains (R_g), the grain boundaries (R_{gb}), and the electrode–electrolyte interfaces (R_{int}).[5,6] However, deconvoluting each of these contributions remains challenging. For example, the high sintering temperatures (over 1000 °C) required to fabricate oxide solid electrolytes make it difficult to control grain sizes and investigate the effect of grain boundaries on Li-ion conductivity.[7–10] Sulfide electrolytes, on the other hand, suffer from side reactions with metallic lithium, resulting in the formation of a continuously evolving solid-electrolyte interphase that complicates the analysis of interfacial resistance and its effects on Li-ion conductivity.[11–15]

Lithium hydroxide halide (Li_2OHX) antiperovskite solid electrolytes are an ideal model system to systematically investigate Li-ion conductivity, as their low melting points (~300 °C) enable them to achieve high relative densities in a single fabrication step.[16] Furthermore, the ability to tune the halogen site chemistry provides a useful tool for controlling their crystal structure. There have been several studies to investigate the Li-ion conductivity in antiperovskite solid electrolytes from the viewpoints of grain boundary, interphase, and grain structure. Li-ion conduction in lithium hydroxide halides was firstly explored as part of the phase-diagram investigation of the LiOH–LiX quasi-binary system.[17,18] The phase transition from orthorhombic to cubic in Li_2OHCl, which occurs at 32 °C, was observed by neutron diffraction analysis.[19] In a similar vein, the effects of proton dynamics on the structural and electrochemical properties of Li_2OHCl have been reported.[20–23] In addition, the relationship between grain boundaries with various orientations and their corresponding activation energies in antiperovskites were reported based on computational simulation.[24,25] Interphase formation of antiperovskite in contact with Li metal at the high temperature of 200 °C was also confirmed by *ex situ* scanning electron microscopy.[26] However, a comprehensive understanding of Li-ion conduction in antiperovskite solid electrolytes that accounts for the combined contribution of grains, grain boundaries, and interphases has not yet been established.

---

[a] *Department of Materials, University of Oxford, Parks Road, Oxford OX1 3PH, UK. E-mail: mauro.pasta@materials.ox.ac.uk*

[b] *Diamond Light Source Ltd., Diamond House, Harwell Science and Innovation Campus, Didcot, OX11 0DE, UK*

[c] *School of Materials Science and Engineering, Kyungpook National University, 80 Daehak-ro, Buk-gu, Daegu 41566, Republic of Korea*

[d] *Chemistry – School of Natural and Environmental Sciences, Newcastle University, Newcastle Upon Tyne, NE1 7RU, UK*

[e] *Centre for Energy, Newcastle University, Newcastle Upon Tyne, NE1 7RU, UK*

† Electronic supplementary information (ESI) available. See **https://doi.org/10.1039/d2ta01462a**

In this study, we conduct a systematic investigation of the Li-ion conductivity in $Li_2OHCl_{1-x}Br_x$ ($x = 0, 0.1, 0.3, 0.5, 0.7, 0.9, 1$) antiperovskite solid electrolytes, with particular emphasis on correlating crystal structure, microstructure, and evolution of lithium-metal–solid electrolyte interphase. X-ray diffraction (XRD) analysis confirms that the ratio of Br to Cl plays a role in determining the crystal structure of $Li_2OHCl_{1-x}Br_x$, which is directly related to Li-ion conductivity in the grain. In addition, we propose that the thermal behavior of Li_2OHX antiperovskite solid electrolytes, which was observed *via in situ* high temperature XRD analysis and differential scanning calorimetry, can serve as a useful descriptor for understanding the structural properties of Li_2OHX antiperovskites. To understand the effect of microstructure on Li-ion conductivity in Li_2OHX antiperovskite solid electrolytes, density functional theory (DFT) calculations were used to capture the difference in the Li-ion mean square displacement (MSD) between grains and grain boundaries, revealing that the Li-ion MSD is significantly reduced at the grain boundary. To experimentally corroborate the contribution of grain boundaries to Li-ion conductivity, we controlled grain size in the material by adjusting the cooling rate during solidification from the melt. To minimize the grain boundary resistance, we fabricated $Li_2OHCl_{1-x}Br_x$ antiperovskite pellets with a melting and solidification process that favored the formation of large grains. By optimizing the compositional and microstructure engineering of the synthesized $Li_2OHCl_{1-x}Br_x$ antiperovskites, we found that the highest room temperature conductivity that could be obtained was 2.52×10^{-3} mS cm^{-1} exhibited by $Li_2OHCl_{0.9}Br_{0.1}$. The $Li_2OHCl_{1-x}Br_x$–Li metal interphase formed at room temperature and 80 °C was also investigated by X-ray photoelectron spectroscopy (XPS) characterization. This study elucidates Li-ion conduction in Li_2OHX antiperovskite solid electrolytes in terms of their crystal structure, microstructure and interphase evolution, thus suggesting a general design strategy for the optimization of Li_2OHX antiperovskite solid electrolytes.

Results and discussion

Synthesis and structural characterization of $Li_2OHCl_{1-x}Br_x$

Lithium hydroxide chloride–bromide antiperovskite solid electrolytes ($Li_2OHCl_{1-x}Br_x$; $x = 0, 0.1, 0.3, 0.5, 0.7, 0.9, 1$) were synthesized from a stoichiometric mixture of precursors at 350 °C based on the following chemical reaction (Fig. S1 and S2†):[27,28]

$$LiOH + (1 - x)LiCl + xLiBr \rightarrow Li_2OHCl_{1-x}Br_x$$

As the name implies, antiperovskite solid electrolytes have the same structural motif as perovskites, but with inverted charges. Specifically, chalcogens, Li-ions, and halogens occupy the octahedral sites, the vertices of $[Li_6O]$ octahedra, and the dodecahedral sites, respectively.[29] In Li_2OHX, Li-ions are substituted by a corresponding number of protons, thus forming Li vacancy sites (Fig. 1a).

The synchrotron XRD patterns of Li_2OHCl and Li_2OHBr are reported in Fig. 1b and c, respectively. Fig. 1b shows that Li_2OHCl is composed of two majority phases, which comprise 52.8 wt% of phase a and 43.4 wt% of phase *b*. Phase *a* has an orthorhombic structure with a space group of $Pmc2_1$ ($a = 3.878$ Å, $b = 3.830$ Å, $c = 8.000$ Å) while phase *b* has a cubic structure with a space group of $Pm\bar{3}m$ ($a = 3.908$ Å), which indicates that there is a large degree of distortion in Li_2OHCl (Fig. 1b, Table S1†).[30–32] In addition, Rietveld refinement of the XRD pattern reveals peaks attributable to 3.7 wt% of LiCl ($Fm\bar{3}m$ space group, $a = 5.148$ Å) while other impurities (*i.e.* Li_2O or LiOH) were barely noticeable, suggesting the presence of Li and Cl vacancies (V'_{Li} and $V^{\bullet}_{Cl}$) in the structure to satisfy charge neutrality.[33] In contrast to Li_2OHCl, Li_2OHBr exhibits a pure cubic structure with a space group of $Pm\bar{3}m$ ($a = 4.047$ Å) at 25 °C (Fig. 1c).

Li_3OX and Li_2OHX are not distinguishable by XRD because of their similar chemical compositions and crystal structures,[22] thus Fourier-transform infrared spectroscopy (FTIR) analysis was conducted (Fig. S3†). A sharp band around 3600 cm^{-1} associated with the O–H stretching vibration was observed for all compositions, which confirms the presence of protons in the $Li_2OHCl_{1-x}Br_x$ system.

The Goldschmidt tolerance factor (t), which describes the degree of distortion in antiperovskites, is defined as follows:[34]

$$t = \frac{R_X + R_{Li}}{\sqrt{2}(R_O + R_{Li})}$$

where R_X, R_{Li} and R_O refer to the ionic radii of the halogen anion, Li-ion and oxygen anion, respectively. As t approaches 1, the ions occupy their lattice sites perfectly, resulting in a highly symmetric structure with a cubic unit cell.[35] The tolerance factor of Li_2OHBr is larger than that of Li_2OHCl due to the large ionic size of Br^-, which supports their experimentally observed crystal structures.[28,36]

The degree of distortion in antiperovskites can be controlled through isoelectronic composition variation.[27,37–40] As is evident from Fig. 1d, even a partial replacement of the Cl in Li_2OHCl with Br, stabilizes the bulk structure of the resulting $Li_2OHCl_{0.9}Br_{0.1}$ because the large Br ion fills the cavity in the framework leading to higher symmetry.[41] The synchrotron XRD patterns confirm this observation, demonstrating the ability of Br to act as an effective structure stabilizer, maintaining a cubic structure at room temperature across all of the tested Br/Cl ratios. Even though each composition contains a small amount of impurities, we preferred to prioritize stoichiometry over purity because of its influence on vacancy concentrations (Fig. S4†).[16,42,43] By comparing the synchrotron XRD patterns of the as-synthesized $Li_2OHCl_{1-x}Br_x$ series, it can be seen that the XRD peaks shift to a lower angle as the Br/Cl ratio increases; this indicates an increase in the lattice parameter because of the larger ionic size of Br^- (Fig. 1e). The lattice parameters of the synthesized antiperovskites are reported in Table S2.† Fitting of the entire XRD patterns across the series indicates that the lattice parameter scales linearly with Br content, following Vegard's law (Fig. 1f).[44]

Pair distribution function (PDF) analysis was employed to further investigate the local structure of the as-synthesized

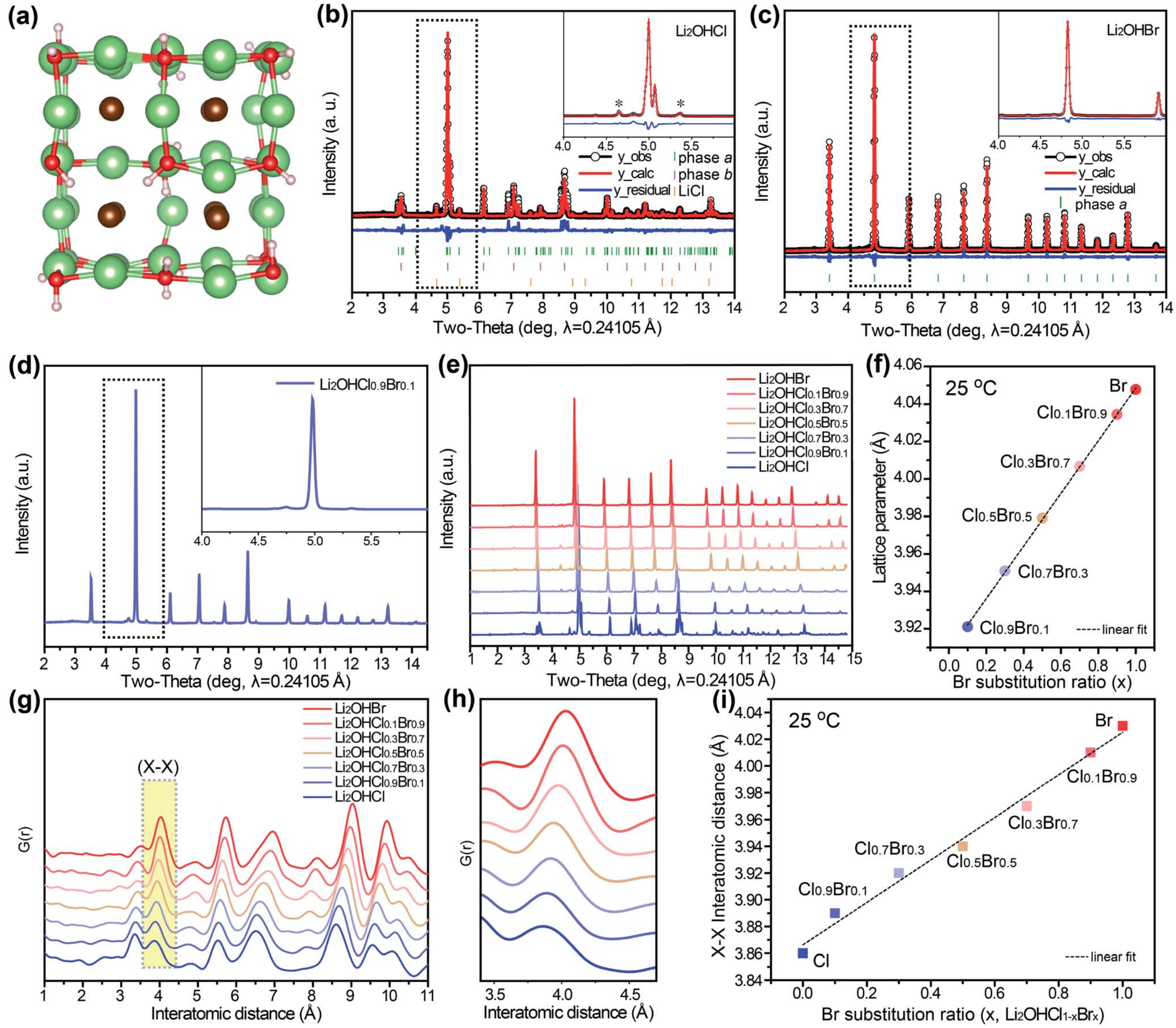

Fig. 1 (a) Crystal structure of lithium hydroxide halide antiperovskite (Li_2OHX). Synchrotron XRD patterns with Rietveld refinements of (b) Li_2OHCl and (c) Li_2OHBr. (d) Synchrotron XRD pattern of $Li_2OHCl_{0.9}Br_{0.1}$. (e) Comparative XRD patterns of as-synthesized $Li_2OHCl_{1-x}Br_x$ ($x = 0$, 0.1, 0.3, 0.5, 0.7, 0.9 and 1) under synchrotron radiation. (f) Lattice parameters of as-synthesized $Li_2OHCl_{1-x}Br_x$. PDF patterns of as-synthesized (g) $Li_2OHCl_{1-x}Br_x$ and (h) their magnified regions assigned to X–X peak and (i) X–X interatomic distances.

$Li_2OHCl_{1-x}Br_x$ series (Fig. 1g).[37] The interatomic distance (X–X (X = Cl or Br)) increases linearly as the proportion of Br increases, as shown in Fig. 1h and i. However, the contribution of the Li–O signal to the PDF pattern was too low to be isolated because of the weak scattering of low-Z ($Z < 10$) atomic species, which makes it difficult to reveal the local structure distortion in the $Li_2OHCl_{1-x}Br_x$ system (Fig. S5†). Here we have shown that traditional room-temperature X-ray analysis using XRD and PDF provides limited useful information on the structural characteristics of $Li_2OHCl_{1-x}Br_x$ because of its lightweight components. Therefore, we investigated the thermal properties of the $Li_2OHCl_{1-x}Br_x$ series to clarify the structural features of these materials.

Thermal properties of $Li_2OHCl_{1-x}Br_x$

Thermal properties of materials can serve as useful indicators of structural characteristics that are difficult to measure directly.[45–47] In order to investigate the thermally-induced structural evolution of the different compositions, *in situ* high temperature XRD measurements were conducted in the temperature range of 25–200 °C under He flow (Fig. 2a and b).

At 40 °C, an orthorhombic-to-cubic phase transition was observed in Li_2OHCl (Fig. 2a). The magnified XRD peak around a two-theta value of 7°, assigned to the (200) orientation, clearly shows the phase transition of Li_2OHCl at 40 °C (Fig. 2a). Above 40 °C, where the cubic antiperovskite phase is stable, a multitude of distinct H positions around the O creates a spherical

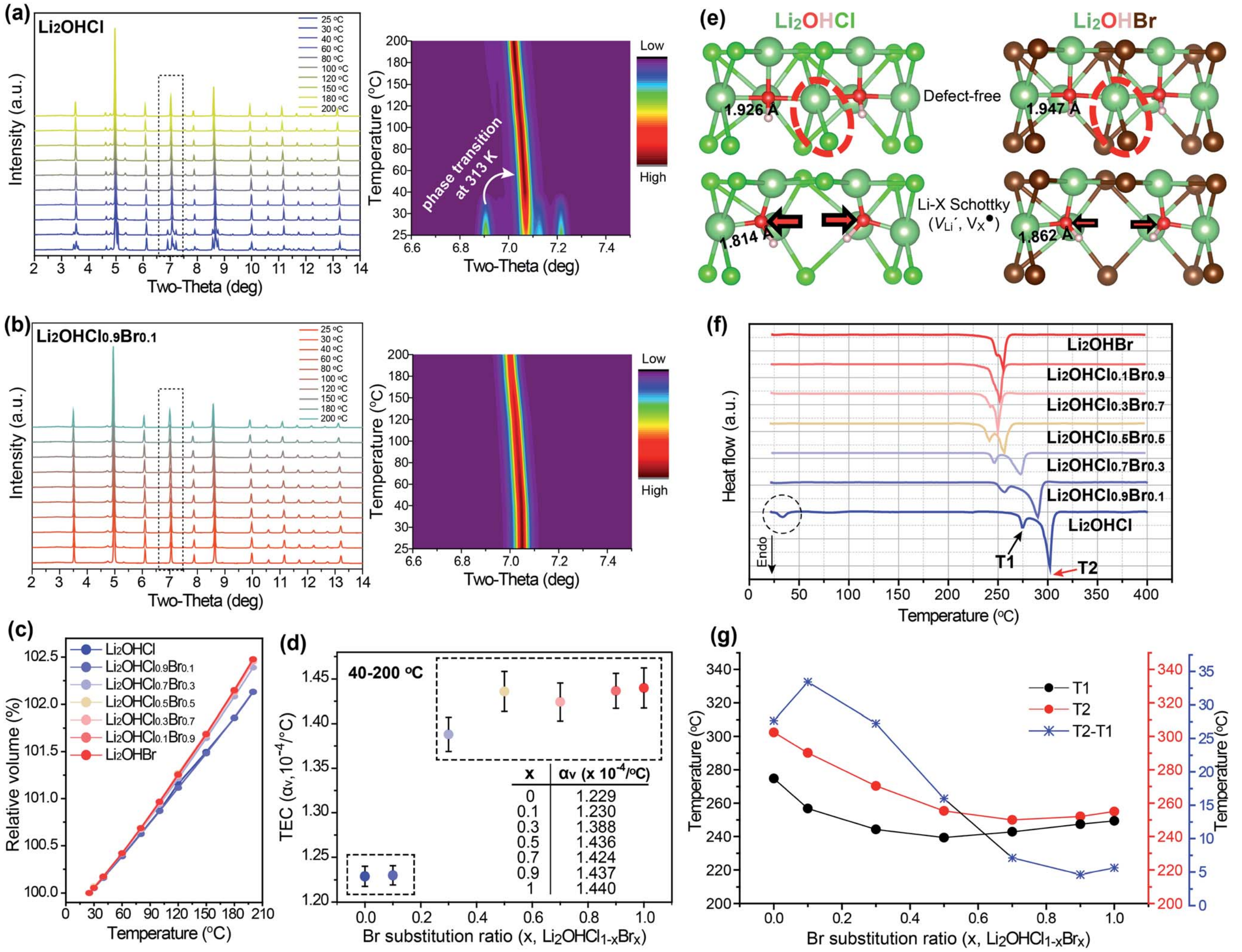

x	αv (x 10⁻⁴/°C)
0	1.229
0.1	1.230
0.3	1.388
0.5	1.436
0.7	1.424
0.9	1.437
1	1.440

Fig. 2 *In situ* high temperature XRD patterns of Li_2OHCl (a) and $Li_2OHCl_{0.9}Br_{0.1}$ (b) with the region around 7 degrees magnified. (c) Relative volume changes for the $Li_2OHCl_{1-x}Br_x$ series with varying Br/Cl ratios. (d) Volumetric thermal expansion coefficients of the $Li_2OHCl_{1-x}Br_x$ series. (e) Schematic illustration of the local structural relaxation resulting from the introduction of a Li–X Schottky defect pair in Li_2OHCl (left) and Li_2OHBr (right). The red arrows denote the movement of the oxygen ion towards its neighbouring Li-ions. (f) DSC profiles of $Li_2OHCl_{1-x}Br_x$ series. (g) Comparison of crystal melting and local disordering temperatures for each composition.

distribution, which facilitates long-range Li-ion diffusion.[21] In contrast to Li_2OHCl, $Li_2OHCl_{0.9}Br_{0.1}$ maintained its cubic structure throughout the entire heating process (Fig. 2b). The other antiperovskite compositions ($Li_2OHCl_{1-x}Br_x$, $x = 0.3$, 0.5, 0.7, 0.9, and 1) described in this work also exhibited stable cubic structures across the whole temperature range (Fig. S6†). The antiperovskite XRD peaks shifted to lower two-theta angles with increasing temperature, indicating thermal expansion of the crystal lattice.

Based on the results of the *in situ* high temperature XRD, changes in the relative volume expansion and the thermal expansion coefficients (TECs) of the synthesized antiperovskites were calculated as shown in Fig. 2c and d respectively. The TECs of the synthesized antiperovskites were calculated for the cubic structures using the equation:

$$\Delta V = \alpha_v V \Delta T$$

where ΔV is the change in unit cell volume, ΔT is the change in temperature, and α_v is the coefficient of expansion (Table S3 and Fig. S7†).[48] The TECs of Li_2OHCl and $Li_2OHCl_{0.9}Br_{0.1}$ are 1.229×10^{-4} and 1.230×10^{-4} °C^{-1}, respectively as calculated using unit cell volumes in the temperature range of 40–200 °C (Fig. 2d). As the Br substitution ratio (x) was increased from 0.1 to 0.3 ($Li_2OHCl_{1-x}Br_x$), the TEC increased from 1.230×10^{-4} to 1.388×10^{-4} °C^{-1} and slightly increased to 1.436×10^{-4} °C^{-1} beyond $x = 0.5$.

Notably, the TEC and the degree of volume expansion of the antiperovskites enabled us to classify these materials into two groups: (1) Li_2OHCl and $Li_2OHCl_{0.9}Br_{0.1}$ which have smaller TECs, and (2) the other antiperovskites with higher Br content with larger TECs. The overall trends of linear TECs (α_L) calculated at 40 and 200 °C were still the same (Fig. S8†). The TEC is inversely proportional to the strength of the bonds between the metal atoms in the materials; however, in this case, the TEC values do not scale linearly with the Br proportion as expected. Instead, they vary in a discontinuous fashion that cannot be explained solely based on the difference in ionicity between Br and Cl.[49–51]

DFT calculations were used to uncover additional structural effects that could result in the observed TECs. We carried out geometry optimizations of Li_2OHCl, $Li_2OHCl_{0.9}Br_{0.1}$ and Li_2OHBr for both the defect-free materials and materials with a single lithium-halide Schottky defect in order observe the effect of this defect pair on the surrounding local structure (Fig. 2e and S9†). We simulate the Li–X (X = Cl or Br) Schottky defect based on the XRD result of Li_2OHCl to reflect the presence of LiCl as a minor impurity. It is known from several previous reports that the formation energy of the Li–O Schottky defect is higher than that of the Li–Cl Schottky defect and was therefore not calculated again here.[52–54] To identify the underlying reason for this discrepancy in the TEC trend, we investigated the local Li–O structure around the lithium-halide Schottky defect pair in all three materials and compared the results to those for the defect-free materials. A consistent decrease in the interatomic distance between nearest-neighbor Li and O ions was observed for all three materials. For Li_2OHBr, the average reduction in the interatomic distance between Li and O ions vicinal to the Schottky defect compared to the defect-free system was 0.085 Å (1.947 to 1.862 Å). For Li_2OHCl and $Li_2OHCl_{0.9}Br_{0.1}$, the decreases were 0.112 (1.926 to 1.814 Å) and 0.090 Å (1.929 to 1.839 Å), respectively. DFT results indicate that decreases in the Li–O interatomic distances around Schottky defects drive the reduction in the lattice parameters of these materials. Based on its thermal expansion behavior, we can speculate that $Li_2OHCl_{0.9}Br_{0.1}$ and Li_2OHCl are defect-rich and have distorted structures. It is difficult to quantify vacancies with X-ray or transmission microscopy because of intrinsic sample limitations (Fig. S10†), therefore TEC serves as indirect evidence to explain the structural characteristics.

To further understand the thermal behavior of $Li_2OHCl_{1-x}Br_x$ antiperovskites, differential scanning calorimetry (DSC) was conducted under Ar flow (Fig. 2f). $Li_2OHCl_{0.9}Br_{0.1}$ did not exhibit any endothermic reactions originating from the phase transition upon heating, indicating that the Br-substituted antiperovskites maintain their cubic structure. On the other hand, a small endothermic peak at 35 °C was observed in Li_2OHCl during the heating process; this corroborates the presence of the orthorhombic-to-cubic phase transition in Li_2OHCl, which was observed using *in situ* high temperature XRD.[55]

The melting points of the different $Li_2OHCl_{1-x}Br_x$ compositions lie in the 250–300 °C range (Fig. 2f). Li_2OHCl and Li_2OHBr were fully molten at temperatures of 302 and 255 °C, respectively. In the DSC profile of Li_2OHCl, a weak peak was observed at approximately 27 °C below the crystal melting point. The presence of two such peaks can be understood as being from two distinct melting points, one at a lower temperature (T_1) and another at a higher temperature (T_2) ascribed to local disordering and crystal melting, respectively.[41,51] Therefore, the difference between these two points (ΔT) indicates the extent of lattice mismatch between the local structure and bulk structure. The peaks for $Li_2OHCl_{1-x}Br_x$ antiperovskites with high Br/Cl ratios converged, leading to much smaller values of ΔT, around 5 to 7 °C, which indicates an increase in the structural uniformity between the local structure and the crystal lattice of Br-rich antiperovskites (Fig. 2g). Based on this observation, it can be concluded that $Li_2OHCl_{0.9}Br_{0.1}$ showed the highest structural disorder of the various antiperovskite compositions.

Effect of microstructure on Li-ion conductivity

The low melting point of the Li_2OHX antiperovskite allows for the facile fabrication of high density pellets in a single step *via* a melting–solidification process[16] (Videos S1 and S2†). In addition, this allows the size of the grains to be controlled by changing the cooling rate of the molten salt. The pellets were cast in a custom stainless steel mold (Fig. 3a). After melting and solidification, the $Li_2OHCl_{0.9}Br_{0.1}$ powder was composed of cube-shaped single-crystal grains, reflecting the cubic crystal symmetry of synthesized $Li_2OHCl_{0.9}Br_{0.1}$ (Fig. 3b). The cross-sectional SEM image of an antiperovskite pellet shows limited porosity (Fig. 3c); its relative density was determined to be 95.8% by the Archimedes method. Higher-magnification SEM images of the pellet cross-section show a compact grain structure with clear grain boundaries. The grain size in both Li_2OHCl and Li_2OHBr is 2–3 μm, and each grain is composed of a single antiperovskite crystallite (Fig. 3d–f). The lack of significant structural differences between the cross-sectional SEM images confirms that the grain size is halogen ion agnostic (Fig. S11†). Cross-sectional SEM images of antiperovskite pellet in this study were obtained from broken pieces without any pretreatment (*i.e.* polishing or Ar^+ ion milling) to minimize sample damage, therefore the change in contrast along grain boundaries originates from a difference in surface topology rather than a change in chemical composition (Fig. S12a†). Energy-dispersive X-ray spectroscopy (EDS) elemental mapping also confirms a homogeneous distribution of the halogen element across grain boundaries (Fig. S12b†). This demonstrates that the melting and solidification process is a facile and effective method for making dense pellets without pressing for both antiperovskites.

DFT calculations were conducted on Li_2OHX to provide insights into how the grain boundaries and microstructure of antiperovskite solid electrolytes affect Li-ion migration. Cubic Li_2OHBr was selected as a model system for DFT calculations to investigate the effect of grain boundaries on Li-ion conductivity in antiperovskites to avoid complications introduced by the phase transition in Li_2OHCl. The optimized configuration of the Σ3(111) coherent twin grain boundary for Li_2OHBr simulated in this study is presented in Fig. 4a. In this structure, the *x* and *y* directions represent the planes of the grain boundaries, while the *z* direction is perpendicular to the grain boundary plane. Full details regarding the choice, construction and properties of this grain boundary are available in the Experimental section. The calculated grain boundary energy of 0.41 J m^{-2} for this structure is similar to the values of 0.34 and 0.29 J m^{-2} obtained for the same grain boundary in dehydrated antiperovskite Li_3OCl from molecular dynamics and DFT, respectively.[24,56] This grain boundary energy is low compared to similar grain boundaries in other typical perovskites, such as $BaTiO_3$ and $SrTiO_3$; this has been previously discussed and is due to the

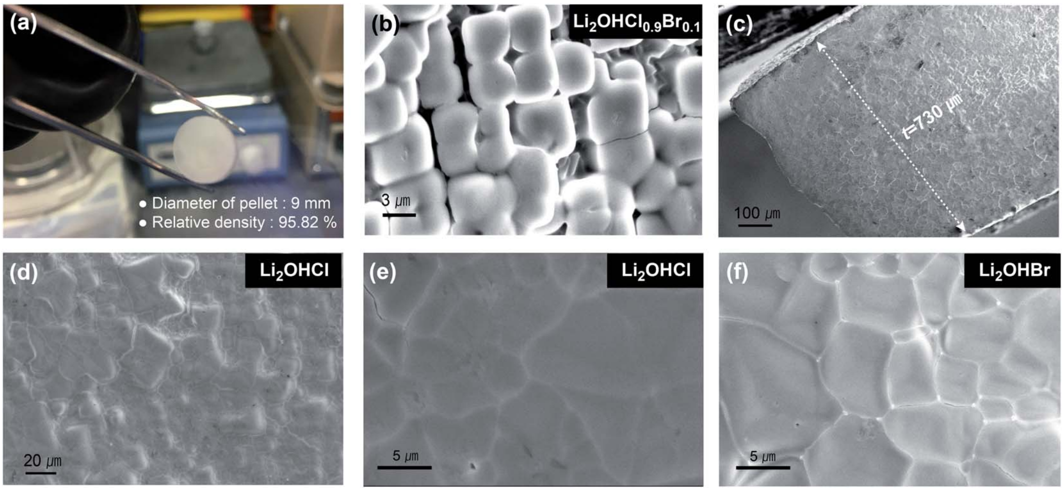

Fig. 3 (a) Digital photograph of Li_2OHBr antiperovskite solid electrolyte fabricated by melting and solidification. (b) The morphology of $Li_2OHCl_{0.9}Br_{0.1}$ powder after melting and solidification. (c) Cross-sectional image of a Li_2OHBr pellet. Grain structure of a Li_2OHCl pellet at (d) low and (e) high magnifications. (f) Grain structure of an Li_2OHBr pellet at high magnification.

relatively small energetic penalty for cleaving Li–O and Li–Cl bonds and the ability of Li to adjust to many different coordination environments.[57] Fig. 4b shows an Arrhenius plot of the calculated Li-ion diffusion coefficients of the grain boundary and grain components of the Li_2OHBr $\Sigma3(111)$ grain boundary. It is clear from this plot that Li-ion diffusion is severely inhibited in the grain boundary compared to the grain. This is further confirmed when we extrapolate the calculated Li-ion diffusion coefficients to room temperature. The Li-ion diffusion coefficients of the grain and grain boundary components of the structure at 300 K are 3.45×10^{-10} and 7.92×10^{-12} cm s^{-1}, respectively. These values reveal that Li-ion diffusion

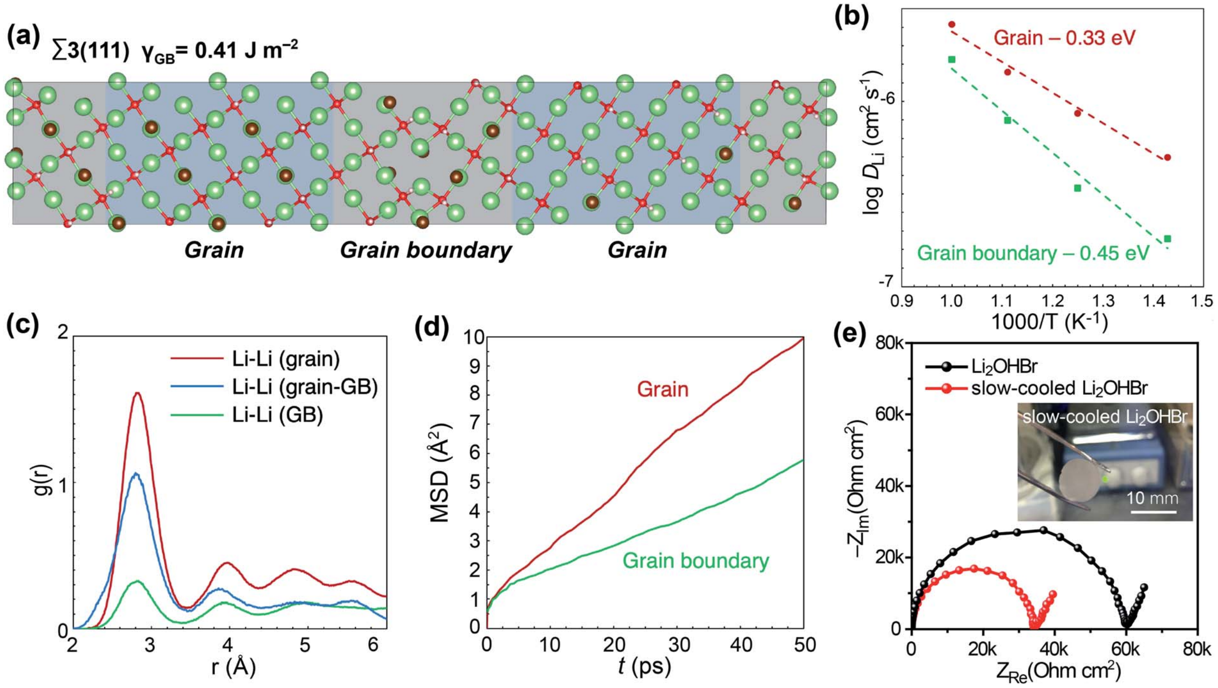

Fig. 4 (a) Structure and energy of the simulated Li_2OHBr $\Sigma3(111)$ grain boundary. (b) Li-ion diffusion (D_{Li}) and activation energies for the grain boundary (GB) and grain components of the Li_2OHBr $\Sigma3(111)$ grain boundary. (c) Radial distribution functions ($g(r)$) for Li–Li ion pairs in the Li_2OHBr $\Sigma3(111)$ grain boundary. (d) Mean squared displacement (MSD) of Li-ions for the grain boundary and grain components of the Li_2OHBr $\Sigma3(111)$ grain boundary at 1000 K. (e) (Inset) digital photograph of a slow-cooled Li_2OHBr pellet. Comparison of EIS spectra of a Li_2OHBr pellet and slow-cooled Li_2OHBr pellet measured at 25 °C.

decreases by almost two orders of magnitude from the grain to the grain boundary at room temperature. The activation energy for the grain boundary is also significantly larger than for the grain (0.45 and 0.33 eV, respectively) which further illustrates the significant grain boundary resistance in Li_2OHBr. Radial distribution functions (RDFs) of Li–Li ion pairs are shown in Fig. 4c to investigate the structural effect of $\Sigma3(111)$ grain boundaries on Li–Li order/disorder, which is expected to have a significant impact on Li-ion diffusion. As indicated by the increase in peak widths, Li-ion disorder increases from more ordered in the grain to less ordered in the grain boundary. While an increase in disorder can result in enhanced Li-ion diffusion in bulk solid electrolytes, at grain boundaries, it prevents intergranular Li-ion diffusion and effectively limits Li-ions in the grain boundary to 2D diffusion pathways. This can be clearly seen from the MSD of Li-ions in the three primary directions for the grain boundary and grain components (Fig. 4d and S13†). In contrast to Li-ion diffusion in the x and y directions, Li-ion diffusion across the grain boundary in the z direction is severely inhibited and is effectively negligible for Li-ions in the grain boundary.

To verify the DFT results, slow-cooled Li_2OHBr pellets were also fabricated. The effect of grain boundaries cannot be isolated by comparing Li_2OHBr pellets fabricated by the melting and solidification process to those prepared by traditional ball-milling and cold-pressing. While this would create differences in the size of grains and number of grain boundaries, it would also result in large differences in both the crystallinity and relative density of the pellets. However, Li_2OHX antiperovskite solid electrolytes present a convenient model material system to study the effect of grain boundaries on Li-ion conductivity due to their low melting points, as the average grain size can be controlled, without affecting relative density (96.3 and 95.8% for slow-cooled and fast-cooled Li_2OHBr pellets, respectively), by simply changing the cooling rate during solidification. As shown in Fig. 4e, the slow-cooled Li_2OHBr pellet is more transparent than the regular Li_2OHBr pellet due to reduced light scattering at the grain boundaries, indicating the formation of larger grains in the slow cooled-pellet. The SEM image of the slow-cooled Li_2OHBr pellet also shows that it has larger grains compared to the fast-cooled sample (Fig. S14†). The conductivity of the slow-cooled Li_2OHBr was 1.99×10^{-3} mS cm^{-1} which is 1.5 times higher than that of Li_2OHBr produced with a the typical cooling rate (Fig. 4e). This validates the results of the DFT calculations by experimentally showing that large grains, and consequently reduced grain boundary resistance, are ideal for achieving high Li-ion conductivity. This is the first experimental validation of the effect of grain boundary on Li-ion conductivity by melting–solidification. Most studies on antiperovskites reported in literature are based on powders that are ball-milled and cold-pressed to make pellets. However, antiperovskite solid electrolytes prepared by such a method exhibit low ionic conductivity, primarily due to the high grain boundary resistance. The melting and solidification process employed here facilitates the formation of larger grains and fewer grain boundaries demonstrating a distinct advantage over traditional ball milling and cold pressing.

Structure–electrochemical property relationship

The combined effect of Br-anion substitution and reduced grain boundary resistance in $Li_2OHCl_{1-x}Br_x$ antiperovskites were assessed by electrochemical measurements of antiperovskite solid electrolytes. Li-ion conductivities and activation energies of $Li_2OHCl_{1-x}Br_x$ were determined by electrochemical impedance spectroscopy (EIS) measurements at various temperatures with Ni blocking electrodes (Fig. 5a–c, S15 and Table S4†).[58,59] Bulk and grain boundary contributions could not be deconvoluted, hence the conductivity represents that of the entire system. While the mechanistic considerations are related to bulk transport, it is reasonable to presume that the grain boundary contributions will not significantly influence the observed trends, as differences in grain structure were minimized by preparing samples using the same cooling rate.[37,60]

At room temperature, the conductivities of Li_2OHCl and Li_2OHBr were 1.93×10^{-3} and 1.29×10^{-3} mS cm^{-1}, respectively. Meanwhile, $Li_2OHCl_{0.9}Br_{0.1}$ exhibited a conductivity of 2.52×10^{-3} mS cm^{-1}, which was the highest of the synthesized $Li_2OHCl_{1-x}Br_x$ series at room temperature (Fig. 5g). Although Br substitution into Li_2OHCl helps to stabilize the overall crystal structure into the more ionically conductive cubic symmetry at room temperature, high Br/Cl ratios lower Li-ion migration because the large size of the Br anion displaces protons from the cubic edge to form bent O–H–Br bonds. In this position, the steric hindrance and coulombic repulsion of the protons impedes the migration of Li-ions.[28]

Li_2OHCl exhibited a change in activation energy from 0.83 to 0.53 eV at 40 °C, again confirming the orthorhombic-to-cubic phase transition of Li_2OHCl. The other antiperovskites showed linear relationships in the Arrhenius plots thus confirming the cubic structures of the Br-substituted antiperovskites (Fig. 5d–f). Within the cubic structures, the activation energy can be divided into two groups; Li_2OHCl and $Li_2OHCl_{0.9}Br_{0.1}$ with smaller activation energies and the other antiperovskites with larger values, as displayed in Fig. 5h. Notably, the change in activation energy with respect to the Br substitution ratio shows almost the same trend as the change in TEC. While the anion lattice softness is linearly proportional to the substitution ratio of Br,[37] the related ionic conductivity and activation energy in this experiment did not follow the expected linear trend with the variation in Br content. This further corroborates the presence of structural disorder and its large influence on both ionic conductivity and activation energy.[61,62] Furthermore, the overall conductivities of Li_2OHX antiperovskites in this study are higher than those reported for antiperovskites fabricated by traditional ball-milling and cold pressing methods.[21,63] These results illustrate how both the chemistry and microstructure of the Li_2OHX antiperovskites can be optimized to improve their conductivity as Li-ion solid electrolytes.

Interphase evolution of $Li_2OHCl_{1-x}Br_x$ antiperovskite solid electrolytes in contact with metallic lithium

In order to evaluate the chemical stability of the synthesized antiperovskites against Li metal, X-ray photoemission

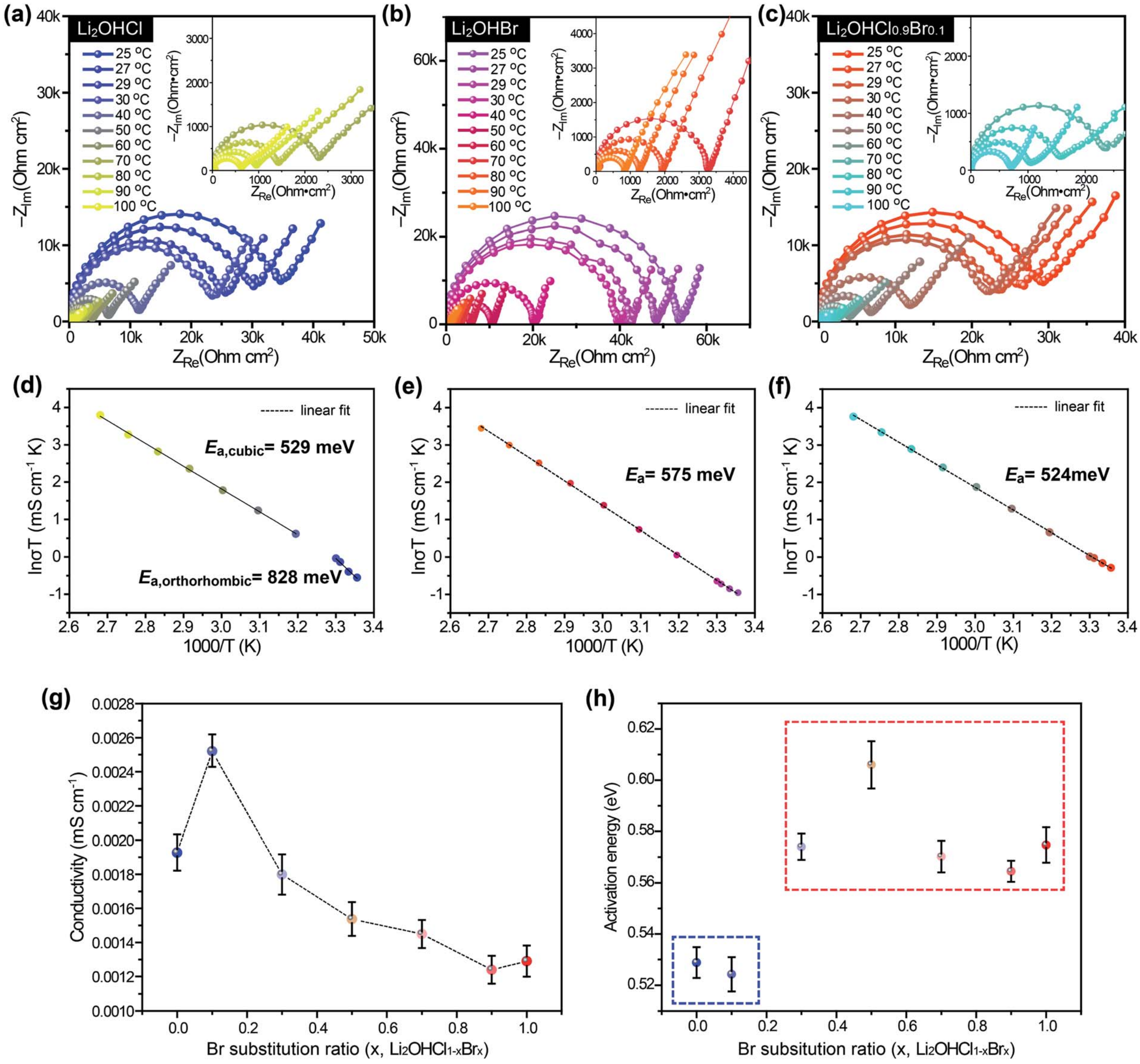

Fig. 5 EIS spectra of (a) Li_2OHCl, (b) Li_2OHBr, and (c) $Li_2OHCl_{0.9}Br_{0.1}$ measured at 25–100 °C using a Ni/Ni symmetric configuration. Arrhenius plots of (d) Li_2OHCl, (e) Li_2OHBr, and (f) $Li_2OHCl_{0.9}Br_{0.1}$ obtained from EIS spectra (g) Comparison of the ionic conductivities of $Li_2OHCl_{1-x}Br_x$ at room temperature. (h) Comparison of the activation energies of $Li_2OHCl_{1-x}Br_x$ under cubic symmetry.

spectroscopy (XPS) was employed. The solid electrolyte interphase (SEI) evolution was monitored at room temperature by conducting *in situ* Li deposition and simultaneously capturing photoemission spectra (Fig. 6a and S16†). For $Li_2OHCl_{0.9}Br_{0.1}$, the intensity of the peak assigned to Li_2O (528.2 eV) increases and the Li 1s peak shifts to a lower binding energy as Li_2O forms with Li metal deposition. Unlike the observed increase in the Li_2O signal intensity, the signals from the Cl 2p and Br 3d species decreased with continued Li deposition, which indicates that Li_2O formation is likely originating from Li^0 reaction with O_2 within the XPS chamber and not as part of the SEI formation.[13] The XPS spectra for both Li_2OHCl and Li_2OHBr exhibited the same trends as $Li_2OHCl_{0.9}Br_{0.1}$ during Li deposition, which indicates their chemical inactivity or negligible reaction upon contact with Li metal at room temperature (Fig. S17 and S18†). The absence of a change in the interfacial resistance of $Li_2OHCl_{0.9}Br_{0.1}$ in contact with Li metal even after 24 h at room temperature, as evidenced by EIS measurements (Fig. 6b), further supports this hypothesis. To investigate the chemical reaction of $Li_2OHCl_{0.9}Br_{0.1}$ in contact with Li metal at elevated temperatures, a $Li_2OHCl_{0.9}Br_{0.1}$ pellet was kept in contact with a Li foil at 80 °C for 7 days. The Li metal layer was then peeled off the pellet, and a depth-profile analysis was conducted on the Li metal using XPS (Fig. 6c). In contrast to the room temperature XPS spectra, the O 1s signal originating from the antiperovskite decreased, whereas the intensity of the Cl 2p remained consistent, which suggests decomposition of the Li_2OHX antiperovskite material when in contact with Li metal at high temperatures based on the following reaction:[26]

$$2Li_2OHX + 2Li \rightarrow 2Li_2O(s) + 2LiX(s) + H_2(g)$$

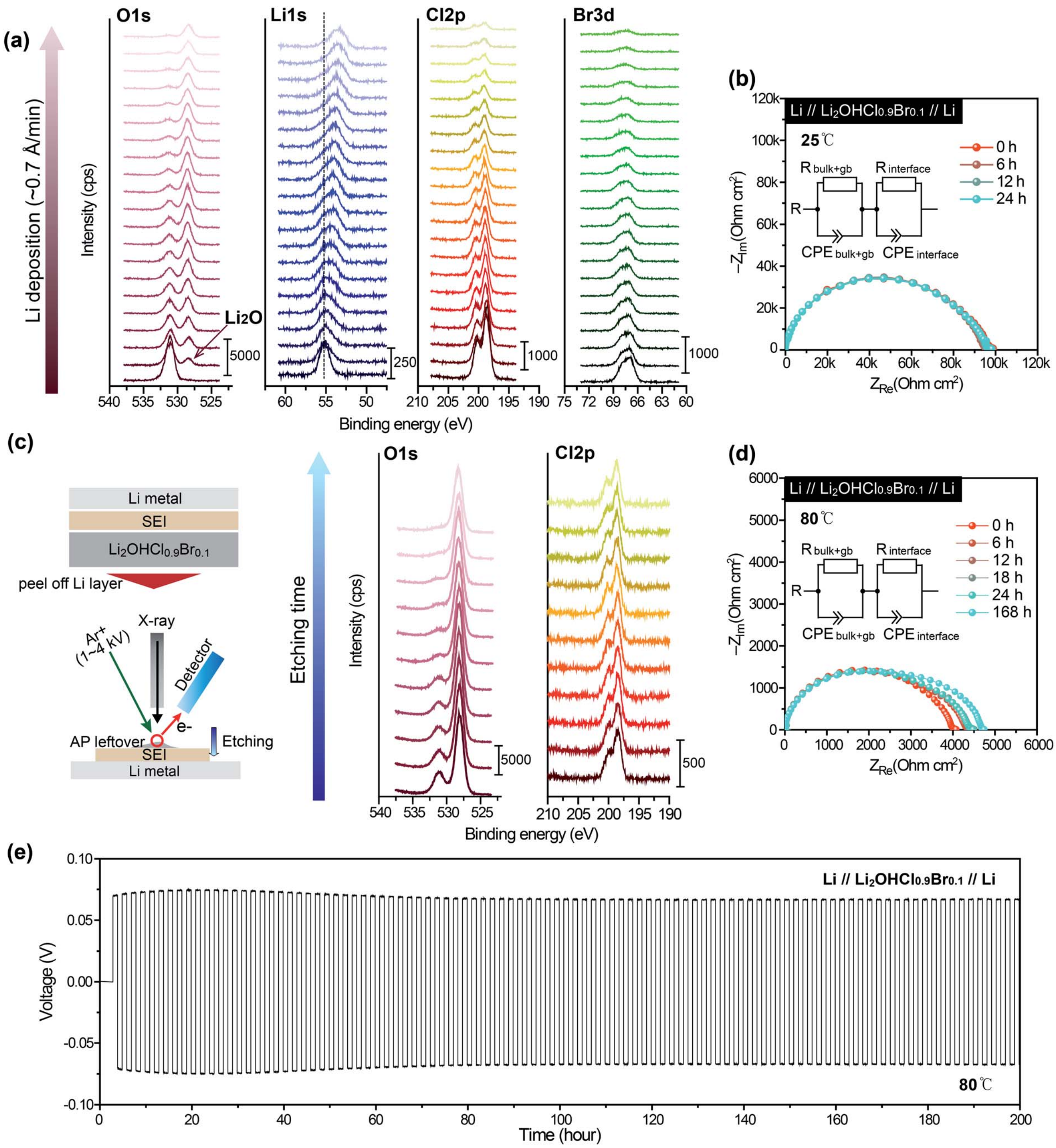

Fig. 6 (a) O 1s, Li 1s, Cl 2p, and Br 3d XPS spectra of a $Li_2OHCl_{0.9}Br_{0.1}$ as a function of increasing lithium metal deposition (from bottom to top) at room temperature. The total thickness of Li metal after deposition is 14 nm. (b) EIS spectra of a symmetric $Li/Li_2OHCl_{0.9}Br_{0.1}/Li$ cell stored for 24 hours at 25 °C. (c) XPS depth profile analysis in the O 1s and Cl 2p regions, collected from Li metal which was in contact with a $Li_2OHCl_{0.9}Br_{0.1}$ at 80 °C. (d)EIS spectra of a symmetric $Li/Li_2OHCl_{0.9}Br_{0.1}/Li$ cell stored for 7 days at 80 °C. (e) Lithium stripping/plating cycling profiles of a $Li/Li_2OHCl_{0.9}Br_{0.1}/Li$ cell at 80 °C.

Moreover, the EIS result of $Li_2OHCl_{0.9}Br_{0.1}$ shows an increase in the interfacial resistance between the solid electrolyte and the Li metal layer to 705 Ω cm^2 after 7 days, indicating the formation of a steadily evolving solid electrolyte–Li metal interphase (SEI) layer at high temperature (Fig. 6d). However, once a stable SEI layer is formed, further reaction between the $Li_2OHCl_{0.9}Br_{0.1}$ antiperovskite and Li within the SEI layer seems to be effectively mitigated, since the voltage profile shape of a Li–Li symmetric cell was fairly stable without a noticeable increase in polarization after 200 h at 80 °C (Fig. 6e).

Conclusions

In conclusion, we have conducted a comprehensive investigation of various factors that affect Li-ion migration in Li_2OHX

antiperovskite solid electrolytes. The Li-ion conductivity was controlled by carefully modulating the crystal structure, microstructure, and interphase evolution. Bromine substitution in halogen sites successfully stabilized the $Li_2OHCl_{1-x}Br_x$ system into the more conductive cubic structure, even at room temperature. Based on EIS analysis, we demonstrate that a stoichiometric substitution of 10% Br is the optimal composition to achieve the highest conductivity within the $Li_2OHCl_{1-x}Br_x$ series. To understand the reason for this, the crystal structure was investigated. However, it is difficult to reveal the structure of these antiperovskites using traditional X-ray analyses due to the presence of lightweight elements such as Li, O and H. Here, we propose that the thermal behavior can effectively serve as a fingerprint to estimate the structural properties of the solid electrolyte that heavily influence Li-ion migration within the material. In conjunction with crystal structure control by chemical substitution, the formation of larger grains by a melting and solidification process reduces grain boundary resistance, and greatly increases ionic conductivities compared to material prepared using traditional ball-milling and cold pressing methods. This process also results in a high relative density of 96% without the need for additional sintering. This study highlights the importance of crystal structure and the utility of advanced processing techniques for the improvement of Li_2OHX antiperovskite solid electrolytes for solid state battery technologies.

Experimental section

Synthesis of $Li_2OHCl_{1-x}Br_x$ ($x = 0, 0.1, 0.3, 0.5, 0.7, 0.9$, and 1)

To obtain the $Li_2OHCl_{1-x}Br_x$, LiOH (98%, Sigma-Aldrich) was mixed with LiCl (≥98%, Alfa Aesar) or LiBr (≥99%, Sigma-Aldrich) in the proper stoichiometric ratio, and ground with a mortar and pestle for 10 min. The precursor was placed on the alumina crucible and heated at 350 °C for 30 min with a ramping rate of 5 °C min^{-1}. The liquid state-$Li_2OHCl_{1-x}Br_x$ was immediately cooled to room temperature, and the resultant chunk was ground with a mortar and pestle to make $Li_2OHCl_{1-x}Br_x$ antiperovskite powder.

Fabrication of antiperovskite pellets

The $Li_2OHCl_{1-x}Br_x$ pellets were fabricated by a melting and solidification process. 0.03 mol of $Li_2OHCl_{1-x}Br_x$ was placed into a lab-made stainless steel mold with a 10 mm diameter. The mold underwent heat treatment at 350 °C for 6 min. Once melted, the mold was immediately cooled down to room temperature and the resultant pellet was taken out from the mold. Slow cooled-Li_2OHBr pellet was fabricated *via* the same procedure, but cooled in the furnace with the cooling rate of 1 °C min^{-1}. The surface of the antiperovskite pellet was polished with 800 and 2500 grit SiC papers. The whole procedure was done in a glovebox with O_2 and H_2O content < 0.1 ppm to prevent air exposure.

Characterization

SEM measurement and scattering analyses. Field emission-scanning electron microscopy (FE-SEM, Zeiss EVO) was employed to observe the cross-section morphology of the $Li_2OHCl_{1-x}Br_x$ pellet. All SEM images were observed in the secondary electron emission mode at an accelerating voltage of 10 kV. Energy-dispersive X-ray spectroscopy (EDS) elemental maps were acquired with an electron beam acceleration voltage of 5 kV and a beam current of 1 nA. Synchrotron X-ray total scattering data were collected at the 17 BM-B beamline at the Advanced Photon Source (APS) ($\lambda = 0.24105$ Å). Li_2OHX antiperovskite powder was loaded in 1.1 mm diameter Kapton capillaries and sealed with quartz wool and polymer clay to prevent air exposure. The whole sample was prepared in the glovebox because of the hygroscopic nature of antiperovskite. For *in situ* high temperature XRD measurements, the powder was placed under He flow. The capillary was maintained at target temperatures (25, 30, 40, 60, 80, 100, 120, 150, 180 and 200 °C) for 6 min to ensure the heat transference and stabilization before obtaining the XRD pattern at each temperature. The whole pattern fitting of XRD data was carried out with GSAS-II software.[64] Pair distribution function (PDF) measurements used a X-ray energy of 51.35 keV ($\lambda = 0.24145$ Å). A Varex 4343 CT imageplate detector (2880 × 2880 pixels and 150 × 150 μm pixel size) was used at a distance of 200 mm. The two-dimensional data were converted to one-dimensional XRD data by using GSAS-II software. PDF results were obtained from a Fourier transformation of the background and Compton scattering corrected total data $S(Q)$ in xPDFsuite software over a Q range of 0.1–13 $Å^{-1}$. The model was refined against the Bragg data. The average structural model with a refined lattice parameter of 4.047 Å was used for the simulation of PDF and partial PDFs data in Fig. S5.† These simulations were performed using the PDFgui software.[65]

XPS analysis

XPS measurement during *in situ* Li deposition. Antiperovskite pellets and Li metal were transferred to the XPS chamber using vacuum transfer vessels to minimize air exposure. XPS spectra were collected using a Phi XPS VersaProbe III with an Al Kα X-ray source. For XPS measurement during *in situ* Li deposition, sputtering of the lithium foil (Sigma-Aldrich, thickness = 750 μm) was performed using an acceleration voltage of 2 kV and an argon ion beam current of 1 μA. The angle between the sputter gun and sample surface was 33°. The estimated sputtering depth rate was 0.7 Å min^{-1}, the Li thickness after deposition was about 14 nm, and the total duration of the experiment was 200 minutes.

XPS depth profiling. In-depth XPS measurements were conducted on the Li metal foil which was in contact with antiperovskite solid electrolyte at 80 °C for 7 days. The accumulated sputtering time was 97 min, and the estimated etching rate was 20–25 nm min^{-1}. Data quantification was performed using CasaXPS software. All spectra were charge-referenced to the disordered C 1s peak at a binding energy of 284.8 eV.

Computational details

Geometry optimization calculations. Density functional theory (DFT) simulations were carried out with the Vienna *Ab* *initio* Simulation Package (VASP).[66] A plane-wave cutoff energy of 550 eV and a *k*-point mesh spacing smaller than 0.05 Å^{-1} were utilized for the geometry optimization calculations. The projector augmented wave method[67] and the PBEsol exchange–correlation functional[68] were employed for all calculations. Bulk Li_2OHCl, $Li_2OHCl_{0.9}Br_{0.1}$ and Li_2OHBr structures consisting of 4 × 4 × 4 supercells (320 atoms) were simulated. It is known that the DFT ground state of Li_2OHCl is a tetragonal structure with all the OH^- groups aligned along a single direction.[22] Therefore, the cubic phase of Li_2OHCl was obtained by heating a cubic system with the tetrahedral alignment of the OH^- groups to high temperature using molecular dynamics to randomly orientate them. The calculated lattice parameters for cubic Li_2OHCl, $Li_2OHCl_{0.9}Br_{0.1}$ and Li_2OHBr are 3.873, 3.885 and 4.001 Å, respectively, in excellent agreement with the XRD results.

Grain boundary construction and modelling. The Σ3(111) coherent twin grain boundary for Li_2OHBr simulated in this study was constructed using coincidence site lattice theory,[69] where two individual grains are tilted by a given angle until their surface planes coincide. The final grain boundary structure has cell dimensions of 9.85, 5.51 and 56.43 Å and contains 240 atoms. The grain boundary energy was converged with respect to grain boundary separation. The grain boundary energy was determined by taking the energy difference between the grain boundary and bulk structures and dividing it by twice the area of the shared interface.[24] As shown in Fig. 4a, the structure was divided into grain boundary and grain regions to calculate their respective contributions to the Li-ion diffusion. These same regions were also used to define the different RDFs in Fig. 4d. The RDFs were produced using the structural information obtained from the *ab initio* molecular dynamics (AIMD) simulations, as described in the next section.

***Ab initio* molecular dynamics calculations.** AIMD simulations were utilized with a plane-wave cutoff energy of 400 eV and the *k*-space was sampled using the gamma-point only. AIMD runs of 50 ps were carried out at 700, 800, 900 and 1000 K using a NVT ensemble with a Nose–Hoover thermostat.[70] These were used to investigate Li-ion transport in the Li_2OHBr grain boundary–grain structure. An AIMD simulation was also carried out at 300 K for 20 ps to obtain the radial distribution functions given in Fig. 4c. A time step of 1 fs was used to account for the motion of the protons. Self-diffusion data for the Li-ions were obtained from the mean square displacement (MSD) according to:

$$\langle r_{\mathrm{i}}^{2}(t)\rangle = 6D_{\mathrm{Li}}t,$$

where $\langle r_{\mathrm{i}}^{2}(t)\rangle$ is the MSD, D_{Li} is the diffusion coefficient for Li-ions and t is time. An example MSD plot for 1000 K is given in Fig. 4d.

Electrochemical measurements

Electrochemical impedance spectroscopy (EIS) measurements were performed using a frequency response analyzer (MTZ, Biologic, France) over the frequency range of 35 MHz to 0.1 Hz with a voltage amplitude of 10 mV at various temperatures of 25, 27, 29, 30, 40, 50, 60, 70, 80, 90 and 100 °C. The temperature was monitored by an internal thermocouple which was connected to a MTZ analyzer. For EIS characterization, a pouch cell was used, using symmetric Ni/Ni and Li/Li cells with $Li_2OHCl_{1-x}Br_x$ antiperovskite solid electrolytes. The Ni blocking electrode was deposited on the surface of the solid electrolyte by RF magnetron sputtering with a power of 50 W, Ar gas flow rate of 10 sccm and sputtering rate of 1.5 A s^{-1}. The thickness of the Ni blocking electrode was 1 μm confirmed by SEM measurement. The Li metal (30 μm thickness, Honjo Metal Co., Ltd) electrodes were 9 mm in diameter, fully covering the surface of the pellet. All cells were assembled and sealed under vacuum in pouches, with Cu foils serving as current collectors. For $Li/Li_2OHCl_{1-x}Br_x/Li$ cells, a pressure of 7 MPa was applied to the pouch cells *via* spring clamps to improve the contact between the Li metal and solid electrolyte. Galvanostatic cycling was performed on the two-electrode cells using a VMP3 at 80 °C. The cycling areal capacity for each Li plating and stripping was fixed at 0.01 mA h cm^{-2}.

Conflicts of interest

There are no conflicts to declare.

Acknowledgements

The authors would like to acknowledge the ISCF Faraday Challenge project SOLBAT [grant number FIRG026] and the Henry Royce Institute (through UK Engineering and Physical Science Research Council grant EP/R010145/1) for capital equipment. We acknowledge technical supports with 17 BM-B beamline at Advanced Photon Source (APS, Contract No. DE-AC02-06CH11357). H. J. Lee acknowledges support from the National Research Foundation of Korea (NRF-2019R1A6A3A03031343). We are grateful to the David Cockayne Center for Electron Microscopy for the use of their electron microscopes. J. A. D. gratefully acknowledges the EPSRC (EP/V013130/1) and Newcastle University (Newcastle Academic Track (NUAcT) Fellowship) for funding. *Via* membership of the UK's HEC Materials Chemistry Consortium, which is funded by the EPSRC (EP/L000202, EP/L000202/1, EP/R029431 and EP/T022213), this work used the ARCHER UK National Supercomputing Service.

References

1 A. Manthiram, X. Yu and S. Wang, Lithium battery chemistries enabled by solid-state electrolytes, *Nat. Rev. Mater.*, 2017, **2**, 16103.

2 J. Janek and W. G. Zeier, A solid future for battery development, *Nat. Energy*, 2016, **1**, 16141.

3 K. Kerman, A. Luntz, V. Viswanathan, Y.-M. Chiang and Z. Chen, Review Practical Challenges Hindering the Development of Solid State Li Ion Batteries, *J. Electrochem. Soc.*, 2017, **164**, A1731–A1744.

4 Q. Zhao, S. Stalin, C. Z. Zhao and L. A. Archer, Designing solid-state electrolytes for safe, energy-dense batteries, *Nat. Rev. Mater.*, 2020, **5**, 229–252.

5 Z. Zhang, *et al.*, New horizons for inorganic solid state ion conductors, *Energy Environ. Sci.*, 2018, **11**, 1945–1976.

6 T. Famprikis, P. Canepa, J. A. Dawson, M. S. Islam and C. Masquelier, Fundamentals of inorganic solid-state electrolytes for batteries, *Nat. Mater.*, 2019, **18**, 1278–1291.

7 A. Sharafi, C. G. Haslam, R. D. Kerns, J. Wolfenstine and J. Sakamoto, Controlling and correlating the effect of grain size with the mechanical and electrochemical properties of Li7La3Zr2O12 solid-state electrolyte, *J. Mater. Chem. A*, 2017, **5**, 21491–21504.

8 I. N. David, T. Thompson, J. Wolfenstine, J. L. Allen and J. Sakamoto, Microstructure and li-ion conductivity of hot-pressed cubic Li7la3Zr2O12, *J. Am. Ceram. Soc.*, 2015, **98**, 1209–1214.

9 E. Yi, W. Wang, J. Kieffer and R. M. Laline, Flame made nanoparticles permit processing of dense, flexible, Li+ conducting ceramic electrolyte thin films of cubic-Li7La3Zr2O12 (c-LLZO), *J. Mater. Chem. A*, 2016, **4**, 12947–12954.

10 Y. Yan, *et al.*, In Situ Polymerization Permeated Three-Dimensional Li+-Percolated Porous Oxide Ceramic Framework Boosting All Solid-State Lithium Metal Battery, *Adv. Sci.*, 2021, **8**, 2003887.

11 Y. Zhu, X. He and Y. Mo, First principles study on electrochemical and chemical stability of solid electrolyte-electrode interfaces in all-solid-state Li-ion batteries, *J. Mater. Chem. A*, 2016, **4**, 3253–3266.

12 W. D. Richards, L. J. Miara, Y. Wang, J. C. Kim and G. Ceder, Interface Stability in Solid-State Batteries, *Chem. Mater.*, 2016, **28**, 266–273.

13 K. N. Wood, *et al.*, Operando X-ray photoelectron spectroscopy of solid electrolyte interphase formation and evolution in Li2S-P2S5 solid-state electrolytes, *Nat. Commun.*, 2018, **9**, 2490.

14 Y. Wang, *et al.*, Facile Design of Sulfide-Based all Solid-State Lithium Metal Battery: In Situ Polymerization within Self-Supported Porous Argyrodite Skeleton, *Adv. Funct. Mater.*, 2021, **31**, 2101523.

15 F. Sun, *et al.*, Clarifying the Electro-Chemo-Mechanical Coupling in Li10SnP2S12 based All-Solid-State Batteries, *Adv. Energy Mater.*, 2022, 2103714.

16 Y. Xiao, *et al.*, Electrolyte melt infiltration for scalable manufacturing of inorganic all-solid-state lithium-ion batteries, *Nat. Mater.*, 2021, **20**, 984–990.

17 P. Hartwig, A. Rabenau and W. Weppner, Lithium hydroxide halides: phase equilibria and ionic conductivities, *J. Less-Common Met.*, 1981, **78**, 227–233.

18 P. Hartwig and W. Weppner, Ionic conductivities of lithium-halide-based quaternary compounds, *Solid State Ionics*, 1981, **3–4**, 249–254.

19 C. Eilbracht, W. Kockelmann, D. Hohlwein and H. Jacobs, Orientational disorder in perovskite like structures of Li2X(OD) (X=Cl, Br) and LiBr D2O, *Phys. B*, 1997, **234–236**, 48–50.

20 A. Y. Song, *et al.*, Understanding Li-Ion Dynamics in Lithium Hydroxychloride (Li2OHCl) Solid State Electrolyte via Addressing the Role of Protons, *Adv. Energy Mater.*, 2020, **10**, 1903480.

21 F. Wang, *et al.*, Dynamics of Hydroxyl Anions Promotes Lithium Ion Conduction in Antiperovskite Li2OHCl, *Chem. Mater.*, 2020, **32**, 8481–8491.

22 J. A. Dawson, *et al.*, Elucidating lithium-ion and proton dynamics in anti-perovskite solid electrolytes, *Energy Environ. Sci.*, 2018, **11**, 2993–3002.

23 D.-X. Ni, *et al.*, Wet Mechanical Milling Induced Phase Transition to Cubic Anti-Perovskite Li2OHCl, *Chin. Phys. Lett.*, 2022, **39**, 028201.

24 J. A. Dawson, P. Canepa, T. Famprikis, C. Masquelier and M. S. Islam, Atomic-Scale Influence of Grain Boundaries on Li-Ion Conduction in Solid Electrolytes for All-Solid-State Batteries, *J. Am. Chem. Soc.*, 2018, **140**, 362–368.

25 K. Shen, *et al.*, Revealing the effect of grain boundary segregation on Li ion transport in polycrystalline anti-perovskite Li3ClO: a phase field study, *Phys. Chem. Chem. Phys.*, 2020, **22**, 3030–3036.

26 Z. D. Hood, H. Wang, A. S. Pandian, J. K. Keum and C. Liang, Li2OHCl Crystalline Electrolyte for Stable Metallic Lithium Anodes, *J. Am. Chem. Soc.*, 2016, **138**, 1768–1771.

27 Y.-S. Lee, S.-Y. Jung and K.-S. Ryu, Electrochemical Stability and Performance of Li2OHCl Substituted by F or Br as Solid-State Electrolyte, *J. Electrochem. Energy Convers. Storage*, 2021, **18**, 021011.

28 Y. Li, *et al.*, Fluorine-Doped Antiperovskite Electrolyte for All-Solid-State Lithium-Ion Batteries, *Angew. Chem., Int. Ed.*, 2016, **55**, 9965–9968.

29 J. A. Dawson, T. Famprikis and K. E. Johnston, Anti-perovskites for solid-state batteries: recent developments, current challenges and future prospects, *J. Mater. Chem. A*, 2021, **9**, 18746–18772.

30 A. Koedtruad, M. A. Patino, N. Ichikawa, D. Kan and Y. Shimakawa, Crystal structures and ionic conductivity in Li2OHX (X = Cl, Br) antiperovskites, *J. Solid State Chem.*, 2020, **286**, 121263.

31 T. Yamamoto, *et al.*, Synthesis of the Metastable Cubic Phase of Li2OHCl by a Mechanochemical Method, *Inorg. Chem.*, 2020, **59**, 11901–11904.

32 J. Howard, Z. D. Hood and N. A. Holzwarth, Fundamental aspects of the structural and electrolyte properties of Li2OHCl from simulations and experiment, *Phys. Rev. Mater.*, 2017, **1**, 075406.

33 A. G. Squires, J. M. Dean and B. J. Morgan, Aliovalent doping strategies for enhancing ionic conductivity in Li3OCl solid electrolytes: a first-principles assessment, *Chemrxiv*, 2021, DOI: **10.26434/chemrxiv-2021-hzrls**.

34 V. M. Goldschmidt, Die gesetze der krystallochemie, *Naturwissenschaften*, 1926, **14**, 477–485.

35 K. Kim and D. J. Siegel, Correlating lattice distortions, ion migration barriers, and stability in solid electrolytes, *J. Mater. Chem. A*, 2019, **7**, 3216–3227.

36 Z. Wang, H. Xu, M. Xuan and G. Shao, From anti-perovskite to double anti-perovskite: Tuning lattice chemistry to achieve super-fast Li+ transport in cubic solid lithium halogen-chalcogenides, *J. Mater. Chem. A*, 2017, **6**, 73–83.

37 Z. Deng, *et al.*, Local structural changes and inductive effects on ion conduction in antiperovskite solid electrolytes, *Chem. Mater.*, 2020, **32**, 8827–8835.

38 H. Fang and P. Jena, Li-rich antiperovskite superionic conductors based on cluster ions, *Proc. Natl. Acad. Sci. U. S. A.*, 2017, **114**, 11046–11051.

39 J. A. Dawson, H. Chen and M. S. Islam, Composition Screening of Lithium- and Sodium-Rich Anti-Perovskites for Fast-Conducting Solid Electrolytes, *J. Phys. Chem. C*, 2018, **122**, 23978–23984.

40 Z. Deng, B. Radhakrishnan and S. P. Ong, Rational composition optimization of the lithium-rich Li3OCl1- xBrx anti-perovskite superionic conductors, *Chem. Mater.*, 2015, **27**, 3749–3755.

41 J. Zheng, *et al.*, Antiperovskite K 3 OI for K-Ion Solid State Electrolyte, *J. Phys. Chem. Lett.*, 2021, **12**, 7120–7126.

42 Y. Yang, J. Han, M. DeVita, S. S. Lee and J. C. Kim, Lithium and Chlorine-Rich Preparation of Mechanochemically Activated Antiperovskite Composites for Solid-State Batteries, *Front. Chem.*, 2020, **8**.

43 M. B. Effat, *et al.*, Stability, Elastic Properties, and the Li Transport Mechanism of the Protonated and Fluorinated Antiperovskite Lithium Conductors, *ACS Appl. Mater. Interfaces*, 2020, **12**, 55011–55022.

44 A. R. Denton and N. W. Ashcroft, Vegard's law, *Phys. Rev. A: At., Mol., Opt. Phys.*, 1991, **43**, 3161–3164.

45 H. D. Megaw, Crystal structures and thermal expansion, *Mater. Res. Bull.*, 1971, **6**, 1007–1018.

46 S. Volkov, *et al.*, Crystal structure and thermal properties of the LixNa1xKZnP2O7 solid solutions and its relation to the MMZnP2O7 diphosphate family, *J. Solid State Chem.*, 2019, **269**, 486–493.

47 M.-A. Son, K.-W. Chae, J. S. Kim and S.-H. Kim, Crystal Structure and Thermal Expansion Coefficient of Cordierite Honeycomb Ceramics, *Phys. Status Solidi A*, 2019, **216**, 1700994.

48 C. Y. Ho and R. E. Taylor, *Thermal Expansion of Solids*, 1998.

49 A. N. Radhakrishnan, P. P. Rao, S. K. Mahesh, D. S. V. Thamp and P. Koshy, Role of bond strength on the lattice thermal expansion and oxide ion conductivity in quaternary pyrochlore solid solutions, *Inorg. Chem.*, 2012, **51**, 2409–2419.

50 S. Shafeie, *et al.*, Tracking of high-temperature thermal expansion and transport properties vs. oxidation state of cobalt between +2 and +3 in the La 2Co 1+z(Ti 1-xMg x) 1-zO 6-system, *J. Mater. Chem.*, 2012, **22**, 16269–16276.

51 J. Zhang, L. Wang, J. Zhu and Y. Zhao, Structural disorder, sublattice melting, and thermo-elastic properties of anti-perovskite Li3OBr under high pressure and temperature, *Appl. Phys. Lett.*, 2020, **117**, 081904.

52 B. Liu, *et al.*, Computational insights into the ionic transport mechanism and interfacial stability of the Li2OHCl solid-state electrolyte, *J. Materiomics*, 2022, **8**, 59–67.

53 Z. Lu, *et al.*, Defect chemistry and lithium transport in Li3OCl anti-perovskite superionic conductors, *Phys. Chem. Chem. Phys.*, 2015, **17**, 32547–32555.

54 R. Mouta, M. A. B. Melo, E. M. Diniz and C. W. A. Paschoal, Concentration of charge carriers, migration, and stability in Li3OCl solid electrolytes, *Chem. Mater.*, 2014, **26**, 7137–7144.

55 Y. Zhao and L. L. Daemen, Superionic conductivity in lithium-rich anti-perovskites, *J. Am. Chem. Soc.*, 2012, **134**, 15042–15047.

56 B. Chen, C. Xu and J. Zhou, Insights into grain boundary in lithium-rich anti-perovskite as solid electrolytes, *J. Electrochem. Soc.*, 2018, **165**, A3946.

57 Z. Rong, *et al.*, Materials design rules for multivalent ion mobility in intercalation structures, *Chem. Mater.*, 2015, **27**, 6016–6021.

58 H. Wen, *et al.*, Sustainable and Superior Heat-Resistant Alginate Nonwoven Separator of LiNi0.5Mn1.5O4/Li Batteries Operated at 55 C, *ACS Appl. Mater. Interfaces*, 2017, **9**, 3694–3701.

59 J. Chai, *et al.*, A high-voltage poly(methylethyl-cyanoacrylate) composite polymer electrolyte for 5 V lithium batteries, *J. Mater. Chem. A*, 2016, **4**, 5191–5197.

60 M. A. Kraft, *et al.*, Influence of Lattice Polarizability on the Ionic Conductivity in the Lithium Superionic Argyrodites Li6PS5X (X = Cl, Br, I), *J. Am. Chem. Soc.*, 2017, **139**, 10909–10918.

61 S. Muy, *et al.*, Lithium conductivity and Meyer-Neldel rule in Li3PO4–Li3VO4–Li4GeO4 lithium superionic conductors, *Chem. Mater.*, 2018, **30**, 5573–5582.

62 R. Chen, *et al.*, Influence of Structural Distortion and Lattice Dynamics on Li-Ion Diffusion in Li3OCl1−x Br x Superionic Conductors, *ACS Appl. Energy Mater.*, 2021, **4**, 2107–2114.

63 M. K. Sugumar, T. Yamamoto, M. Motoyama and Y. Iriyama, Tailoring the Lithium-ion Conductivity of Li 2 OHBr by Substitution of Bromine with Other Halogens, *Chem. Lett.*, 2021, **50**, 448–451.

64 B. H. Toby and R. B. Von Dreele, GSAS-II: the genesis of a modern open-source all purpose crystallography software package, *J. Appl. Crystallogr.*, 2013, **46**, 544–549.

65 C. L. Farrow, *et al.*, PDFfit2 and PDFgui: computer programs for studying nanostructure in crystals, *J. Phys.: Condens. Matter*, 2007, **19**, 335219.

66 G. Kresse and J. Furthmller, Efficient iterative schemes for ab initio total-energy calculations using a plane-wave basis set, *Phys. Rev. B: Condens. Matter Mater. Phys.*, 1996, **54**, 11169–11186.

67 P. E. Blchl, Projector augmented-wave method, *Phys. Rev. B: Condens. Matter Mater. Phys.*, 1994, **50**, 17953–17979.

68 J. P. Perdew, *et al.*, Restoring the Density-Gradient Expansion for Exchange in Solids and Surfaces, *Phys. Rev. Lett.*, 2008, **100**, 136406.

69 L. Priester, *Grain Boundaries: from Theory to Engineering*, Springer Science & Business Media, 2012.

70 D. J. Evans and B. L. Holian, The NoseHoover thermostat, *J. Chem. Phys.*, 1985, **83**, 4069–4074.